2018

Internal Gravity Wave Detection During The 21 August 2017 Total Solar Eclipse

Michael J.W. Stewart
University of South Carolina

Recommended Citation

Stewart, M. J.(2018). *Internal Gravity Wave Detection During The 21 August 2017 Total Solar Eclipse.* (Master's thesis). Retrieved from https://scholarcommons.sc.edu/etd/4717

INTERNAL GRAVITY WAVE DETECTION DURING THE 21 AUGUST 2017 TOTAL SOLAR ECLIPSE

by

Michael J.W. Stewart

Bachelor of Science
University of Georgia, 2016

Submitted in Partial Fulfillment of the Requirements

For the Degree of Master of Science in

Geography

College of Arts and Sciences

University of South Carolina

2018

Accepted by:

April Hiscox, Director of Thesis

Jean Ellis, Reader

Gregory Carbone, Reader

Cheryl L. Addy, Vice Provost and Dean of the Graduate School

ACKNOWLEDGEMENTS

I would first like to sincerely thank my thesis advisor, Dr. April Hiscox, and committee members, Dr. Jean Ellis, and Dr. Gregory Carbone for their patience, guidance, support, and more than helpful feedback throughout this invaluable experience. Their doors were always open every step of the way to offer helpful comments, engaging discussion, and share stories that offered a peace of mind for a graduate student finding his way.

I would also like to express my sincere indebtedness to those involved in the field project for this research project: Raelene Campbell, Dr. Greg Carbone, Erika Chin, Dr. Jean Ellis, Michelle Harris, Brody Marino, Alex McCombs, Sean McGill, Dr. Caroline Nagel, Georgia Nagel, Patrick Remson, Mayra Román-Rivera, Nicholas Sokol, Hannah Svonkin, and Pete Tereszkiewicz.

Finally, I would like to thank my friends and family, as this thesis would not at all be possible without their unwavering support and encouragement.

ABSTRACT

Total solar eclipses supply both visual captivation and a controlled meteorological experiment through a sudden decrease in solar radiation. However, along with commonly expected changes in weather conditions, prior research suggests an adjustment of atmospheric dynamics caused by both a decrease in local incident solar radiation and the Moon’s sweeping shadow across the Earth at supersonic speed. The result is the potential production of internal gravity waves, which transfer both energy and momentum vertically to and from the upper levels of the atmosphere. A series of radiosondes were launched before, during, and after the 21 August 2017 eclipse in Batesburg, South Carolina. Observations of internal gravity waves and low level meteorological conditions are reported. Finally, the eclipse event is compared to model output which accounts for the solar eclipse. On this occasion, it is concluded that internal gravity waves were sourced from both localized convection to the southeast of the field site location as well as the total solar eclipse. Furthermore, the wave period of the proposed solar eclipse induced internal gravity waves fall in line with previous studies.

TABLE OF CONTENTS

ACKNOWLEDGEMENTS iii

ABSTRACT iv

LIST OF FIGURES vii

CHAPTER I INTRODUCTION 1

CHAPTER II DATA AND METHODS 5

  2.1 DATA COLLECTION 5

  2.2 IDENTIFYING INTERNAL GRAVITY WAVES 8

CHAPTER III NUMERICAL WEATHER PREDICTION 11

CHAPTER IV RESULTS 13

  4.1 SYNOPTIC CONDITIONS 13

  4.2 BOUNDARY LAYER MEASUREMENTS 14

  4.3 INTERNAL GRAVITY WAVE MEASUREMENTS 16

  4.4 WRF SIMULATION 19

CHAPTER V DISCUSSION 22

CHAPTER VI CONCLUSION 26

REFERENCES 28

APPENDIX A WRF PARAMETERIZATION OF SHORTWAVE RADIATION 30

APPENDIX B WRF SHORTWAVE RADIATION PACKAGE ADJUSTED FOR ECLIPSE PATH 32

LIST OF FIGURES

Figure 2.1 Field site location is located south of Lake Murray. While forested, measurements were taken within a cleared and open field 6

Figure 3.1 WRF model domains 11

Figure 4.1 (Left) Synoptic pattern shows the jet stream in northern United States/southern Canada; the ridge pattern over the southeastern United States allows for much weaker wind speeds to impede analysis of balloon ascent. (Right) Surface analysis for 11AM EDT...13

Figure 4.2 Temperature observations with height throughout the boundary layer. Profiles smoothed with low-pass median filter 14

Figure 4.3 Wind magnitude with height throughout the boundary layer. Profiles smoothed using low-pass median filter 14

Figure 4.4 Wind perturbations for launch 1...16

Figure 4.5 Hodograph plot for launch 1...16

Figure 4.6 Wind perturbations for launch 5...17

Figure 4.7 Hodograph plot for launch 5...17

Figure 4.8 Wind perturbations for launch 6...18

Figure 4.9 Hodograph plot for launch 6...18

Figure 4.10 Wind perturbations for launch 8...19

Figure 4.11 Hodograph plot for launch 8...19

Figure 4.12 Temperature and dewpoint from launch 1 is compared to a modeled simulation for the same time frame 20

Figure 4.13 Observed and simulated boundary layer profiles shortly after totality occurred..21

Figure 5.1 Displays the incoming shortwave radiation from 11AM-7PM EDT on 21 August 21, 2017. Associated balloon launches are marked with notes on temperature and wind magnitude measurements...22

CHAPTER I

INTRODUCTION

Solar eclipses occur when the moon passes between the plane of the sun and the Earth. By obscuring the sun’s intense light, the moon’s shadow travels across the landscape and supplies both a visual captivation and a controlled meteorological experiment. A rare event, total solar eclipses occur on average once every approximately 18 months, visible somewhere on the Earth. Furthermore, a specific location can expect subsequent events anywhere between 360 and 410 years (Steel, 2001). By blocking the sun’s solar disc, the moon inhibits the Earth from receiving incoming solar radiation for a short period of time, causing a decrease in surface temperatures (R. C. Anderson et al., 1972). Changes in surface temperature moves the air’s water vapor content closer to saturation, increasing its relative humidity (Gray & Harrison, 2016; Paramitha et al., 2017). The change in surface temperatures also alters atmospheric stability, as noted by observations in Founda et al. (2007). In addition to the sensible and more easily measured changes solar eclipses cause, these events also have the potential to disrupt the atmosphere’s dynamics.

Dating back to the total solar eclipse of 1 January 1889, atmospheric measurements were taken at Willows, California (Upton et al., 1893). While several eclipse events were studied in the years following (Kimball & Fergusson, 1919; Clayton, 1901), eclipse meteorology gained traction when surface and upper air measurements were taken during and after the 7 March 1970 eclipse (R. C. Anderson et al., 1972). Given the rarity of total solar eclipse events over observable surfaces, quantitative information is still scarce, and extrapolation of results is limited. Thus, atmospheric impacts are hard to definitively attribute to eclipse events. A change in atmospheric stability has implications on the mechanical mixing occurring in the atmospheric boundary layer. A decrease in turbulent mixing and a decrease in wind speed were noted in Founda et al. (2007). By contrast, Eaton et al. (1997) did not observe changes in wind speed which exceeded natural variability; however, Krishnan et al. (2004) detected pronounced eclipse-induced changes in wind characteristics. Some studies report sudden gusts of wind during a total eclipse event (Aplin et al., 2016). It is clear that atmospheric effects of solar eclipses are unique at different seasons, different time of the day, and different locations (Founda et al., 2007). These conflicting findings detail the complexity of sudden changes in incoming radiation on atmospheric dynamics and support the need for consistent observations of total solar eclipses.

Perhaps the most interesting debate rests in the existence of eclipse induced internal gravity waves (IGW). IGW influence turbulence near the surface and can aid in supplemental vertical motion to enhance or even trigger localized mesoscale weather events (Bluestein, 1992). IGW are commonly generated through various mechanisms such as frontal patterns, topographic influences, localized convective activity, or jet stream excitation (Fritts, 2003). However, Chimonas and Hines (1971) postulated that the lunar shadow on the surface of the Earth acts to cool the air relative to the surrounding warmer air. This cooler, more dense air sinks, and its momentum brings the surrounding warmer air towards the surface. The air’s adjustment back to thermodynamic equilibrium results in the development of IGW in a V-shaped region behind the shadow (Chimonas & Hines, 1971). Since then, a number of observations have attempted to validate this hypothesis (Anderson, 1999; Aplin et al., 2016; Aplin & Harrison, 2002; Chimonas & Hines, 1971; Eaton et al., 1997; Hobson, G.L. Goodwin & G.J., 1978; Marlton et al., 2016)

One indicator of IGW is the rhythmic oscillation of surface pressure. Previous studies have employed microbarographs to detect small and subtle changes in pressure, on the order of 2 microbars (Chimonas & Hines, 1970). Anderson et al. (1972) utilized this methodology in an open field during a total solar eclipse in the southeastern United States for the 7 March 1970 solar eclipse and measured the primary wave period of 89-minutes. However, instrumentation error left the conclusion of the study open. The 23 October 1976 eclipse was studied using a network of four microbarographs along the southern Australia coast, producing a wave period of 23-minutes and amplitude of 0.001-0.002 millibars (Hobson & Goodwin, 1978). Additional studies were conducted using microbarographs to detect IGW during the 1973, 1999, and 2006 total solar eclipses, yielding wave periods ranging from 20 to 50 minutes (R. C. Anderson & Keefer, 1975; Aplin & Harrison, 2002; Zerefos et al., 2007).

More recently, radiosondes have been used to detect IGW in the upper atmosphere through variations in temperature, wind magnitude and direction, and ascent speed (Marlton et al., 2016). Furthermore, wave periodicity and direction of propagation can be calculated from these metrics (Vincent & Alexander, 2000). Marlton et al. (2016) used this method but was unable to find evidence suggesting eclipse induced IGW by reason of cloud cover and time of year at the higher latitudes of the United Kingdom.

The work presented here uses radiosondes to detect IGW during the 21 August 2017 total solar eclipse in the southeastern United States. This study takes advantage of little cloud cover near Batesburg, South Carolina, near the end of the path of the Great American Eclipse. The remainder of this paper is structured as follows: Chapter 2 details the field campaign, Chapter 3 discusses modeling efforts, Chapter 4 highlights results, and Chapter 5 discusses results.

CHAPTER II

DATA AND METHODS

2.1 DATA COLLECTION

The total solar eclipse of 21 August 2017 spanned the entire continental United States. Lincoln Beach, Oregon witnessed the beginnings of the partial eclipse with totality lasting 1 minute and 59 seconds. The eclipse shadow continued its southeast track towards Carbondale, Missouri; where the greatest duration of totality was observed: 2 minutes and 40 seconds. McClellanville, South Carolina witnessed the end of the partial eclipse at 20:11 UTC (4:11 PM EDT) after a totality which lasted 2 minutes and 34 seconds. The width of the umbra ranged from 70-115 kilometers, with a width of 115 kilometers at the measured site used here.

To measure the evolving atmosphere during the total solar eclipse, eight radiosonde measurements were taken during various stages of the event near Delmar, South Carolina (34.06°N, 81.59°W). This field site is located approximately 32 miles west of Columbia, South Carolina and is located along in the path of totality, 3.2 miles from the shadow centerline. This site was selected to remove urbanization effects from Columbia, which could lead to erroneous low-level measurements, as well as to maximize the length of totality experienced (Collier, 2006). The launch site was an open field located on the fringe of Lake Murray and afforded the maximum duration of totality at 2 minutes and 36 seconds while providing a homogenous landscape to reduce instrument variation (Figure 1). The field site is located within a forested region, but measurements were taken within an open field.

Figure 2.1: Field site location is located south of Lake Murray. While forested, measurements were taken within a cleared and open field.

A series of radiosondes were launched before, during, and after the eclipse to capture the atmospheric responses in temperature, dewpoint, and wind magnitude and direction. These values are sampled at a temporal resolution of 1 second and a spatial resolution of ~2-5.5 meters; this spatial resolution varies depending on the balloon's ascent rate. Each balloon was launched at specific moments during the eclipse to measure changing conditions. Launch timing matched that of several other schools along the eclipse; collectively the measurement created a nationwide dataset showing meteorological response for each specific moment relative to the local eclipse. Each balloon train used a 200-gram Kaymont balloon, an iMet ABxx radiosonde, and Intermet systems software. Balloons were filled with 1.02 cubic meters of helium to achieve a balloon ascent rate of 5 m/s. This rate was selected to safeguard the instrument from oversample in the event of a slower ascent rate and to prevent faster ascent speeds from creating turbulence, which would periodically lead to a slower ascent rate (Sandford *et al*., 2013). The radiosonde relayed information to a file repository within iMet's proprietary software, iMetOS II, via radio antenna and receiver. Table 1 summarizes the balloon launch times relative to the eclipse event as well as details the maximum height and average ascent rate achieved. An additional launch was conducted when radio contact was quickly lost after the release of the third balloon. In addition to the radiosondes, a ground station recorded temperature to verify radiosonde measurements and for ancillary information.

Table 2.1: Launch durations with corresponding contacts of the total eclipse and maximum height achieved.

Balloon Launch	**Time (EDT)**	**Eclipse Contact**	**Height Achieved**	**Average Ascent rate**
1	11:21 A.M. -12:38 P.M.	Pre-eclipse	23,789 meters	5.099 m/s
2	1:06 P.M. – 1:18 P.M.	Start of 1st contact	3,857 meters	5.214 m/s
3	2:04 P.M. – 2:05 P.M.	1st contact	321 meters	5.238 m/s
4	2:19 P.M. – 2:25 P.M.	1st contact	1,656 meters	4.857 m/s
5	2:33 P.M. – 2:52 P.M.	2nd contact/totality/3rd contact	5,353 meters	4.904 m/s
6	2:57 P.M. – 3:20 P.M.	3rd contact	7,080 meters	5.199 m/s
7	4:27 P.M. – 5:40 P.M.	Directly after 4th contact	21,897 meters	4.961 m/s

8	5:51 P.M. – 7:07 P.M	Post-eclipse	21,758 meters	4.790 m/s

2.2 IDENTIFYING INTERNAL GRAVITY WAVES

To detect IGW, a low pass filter is applied to the radiosonde data to remove the periodic sway the radiosonde followed below the balloon. Wind direction and speed are then used to calculate the zonal and meridional components of the wind as well as ascent rate:

Eq.1

$$u = -|w_m| \times sin\left[\frac{\pi}{180} \times w_d\right]$$

Eq. 2

$$v = -|w_m| \times cos\left[\frac{\pi}{180} \times w_d\right]$$

Eq. 3

$$w = \frac{\Delta z}{\Delta t},$$

where w_m is the magnitude of the wind vector and w_d is the meteorological direction of the wind in degrees. Following these calculations, the ascent rate can be calculated from equation 3, where *z* is the altitude above ground level at time *t*. Following the methodology outlined in Vincent and Alexander (2000), a second-order polynomial is fit to the *u*, *v*, and *w* profiles. These polynomials represent the average values of the variables throughout the atmospheric column. Next, the mean observations are subtracted from the true observations, yielding the perturbations in each direction *u'*, *v'*, and *w'*, respectively. The *u'* and *v'* components are then plotted against one another in a hodograph plot. From airy wave theory, an ideal IGW signature would produce a hodograph with an ellipse shape (Massel, 2015).

Further analysis is performed to calculate the vertical wavelength and frequency of the associated IGW using the perturbations *u'*, *v'*, and *w'*. The parcel displacement in each direction, *x'*, *y'*, and *z'*, can be calculated by integrating parcel velocity with respect to time. Because the temporal resolution of the instrument recorded observations every 1 second, the displacement is calculated as the change in speed over the change in time. Next, the maximum displacement in all directions can be determined. Equation 4 represents the maximum displaced parcel of air under the effect of IGW.

Eq 4

$$S = \sqrt{x'^2 + y'^2 + z'^2}$$

By plotting the function, S, against the height, local maxima can be distinguished, allowing for both determination of vertical wavelength of IGW calculation of the wave's intrinsic angular frequency. By selecting the height level in which the maximum displacement perturbation was observed, the parcel's associated *x'*, *y'*, and *z'* displacement can be associated with the IGW's movement. Equation 5 is used at the local maxima detailed in the *S* function to calculate the wave frequency of the internal gravity waves,

Eq 5

$$\omega^2 = f^2 sin^2(\alpha) + N^2 cos^2(\alpha),$$

where *f* is the Coriolis parameter, and α is a function of the displaced parcel, seen in Equation 6,

Eq 6

$$\alpha = tan^{-1}\left(\frac{\sqrt{x'^2+y'^2}}{|z'^2|}\right).$$

Equation 7, *N*, serves as the Brunt–Väisälä frequency, where θ is potential temperature, z is height above ground level, and g is Earth's gravitational constant.

Eq 7

$$N = \sqrt{\frac{g}{\bar{\theta}}\frac{\partial \theta}{\partial z}}$$

By solving for intrinsic angular frequency, IGW periodicity can be solved to yield values in the expected range of 9-90 minutes (Anderson & Keefer, 1975; Goodwin & Hobson, 1978; Aplin & Harrison, 2003; Farges *et al*., 2003). Marlton *et al*. (2016) used this methodology within the height window of 13-17 kilometers. However, it is noted that higher atmospheric windows are more preferable, as the continued decrease in atmospheric density allows for wave amplitudes to increase at a quasi-exponential rate (Marlton *et* al., 2016). Therefore, the atmospheric window of interest is set to be between 16-24 kilometers.

CHAPTER III

NUMERICAL WEATHER PREDICTION

To compare eclipse observations to non-eclipse conditions not afforded to instruments, numerical weather prediction was utilized to consider how much of an impact the total solar eclipse had on atmospheric variables. Weather Research and Forecast (WRF) was used to simulate the non-eclipse of 21 August 2017 with the use of North American Regional Reanalysis (NARR) data. The radiosonde observations are then compared to numerical weather prediction model, WRF.

The WRF run takes advantage of the model's ability to solve for high resolution domains. The largest domain, D1, runs at a 30-kilometer resolution and spans 24-42°N

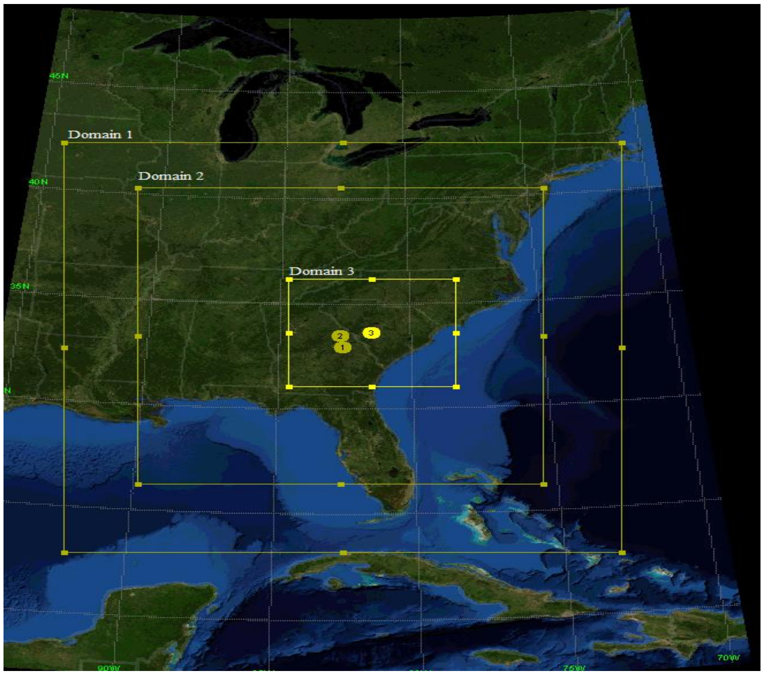

Figure 3.1: WRF model domains

by 69-92°W. The second domain, D2, covers the area bounded by 39.5-26.5°N by 71.5-89.5°N and runs as a 10-kilometer resolution. Finally, a much smaller domain, D3, encompasses a majority of South Carolina and is centered on the field site location. D3 runs at a 1-kilometer resolution and spans 33.1-35°N by 79.2-82.3°W (Figure 1). The model is run on a 30-minute time step.

To avoid a model spin-up error, the model initializes at 21Z (5PM EDT), 20 August 2017 and continues its run until 00Z (8PM EDT), 22 August 2017 (Founda *et al*., 2007); this is 19 hours before the start of the partial eclipse and 4 hours after the end of the partial eclipse. The model initializes with the 32-kilometer North American Regional Reanalysis (NARR) dataset. Model parameterizations for surface layer physics, TKE, microphysics, longwave, and shortwave radiation implements the Monin-Obukhov, MYJ, Ferrier, RRTM, and Dudhia schemes, as outlined in Founda *et al*. (2007).

CHAPTER IV

RESULTS

The path of totality during the 21 August 2017 total solar eclipse pushed across the continental United States. At the field location in Delmar, 100% totality was experienced. Figure 1 details both the area of totality as well as areas outside of totality.

4.1 SYNOPTIC CONDITIONS

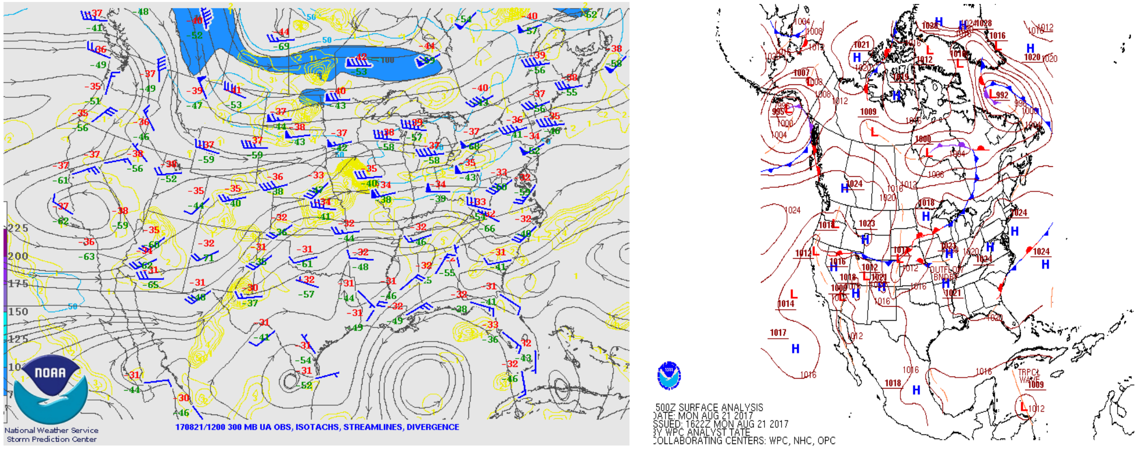

Figure 4.1: (Left) Synoptic pattern shows the jet stream in northern United States/southern Canada; the ridge pattern over the southeastern United States allows for much weaker wind speeds to impede analysis of balloon ascent. (Right) Surface analysis for 11AM EDT (NOAA Storm Prediction Center Archive)

To capture weak atmospheric perturbations caused by IGW, meteorological conditions should be weakly forced from atmospheric dynamics. Given the time of year, the strong winds of the polar jet were well to the north (Figure 3). This is ideal because the polar jet is needed to form cyclonic storms. These cyclonic storms are home to cold and warm fronts, which cause variations in temperature and wind speed and direction and could ultimately muddy the wind direction and magnitude signal solely caused by IGW. A surface analysis (Figure 3) shows a stationary front east of the field site, just off the South Carolinian coastline and extending northeast and off the North Carolinian coast. This feature provided scattered rain showers south of the field site, with localized convective storms becoming more isolated moving northwest from the front.

4.2 BOUNDARY LAYER MEASUREMENTS

To assess the effects the eclipse had on near surface variables, balloon observations are compared to each other through time. Temperature and wind speed and direction are assessed and compared at the surface, 500 meters, 1,000 meters, 1,500 meters, and at the height of the planetary boundary layer at 2,000 meters. A height window of each radiosonde profile was selected to observe changes in temperature and wind speed in the atmospheric boundary layer. This window spanned from the surface to 1,500 meters. Figure 5a and 5b show a profile of each balloon launch and associated changes in the temperature and wind speed with height up to 1500 meters.

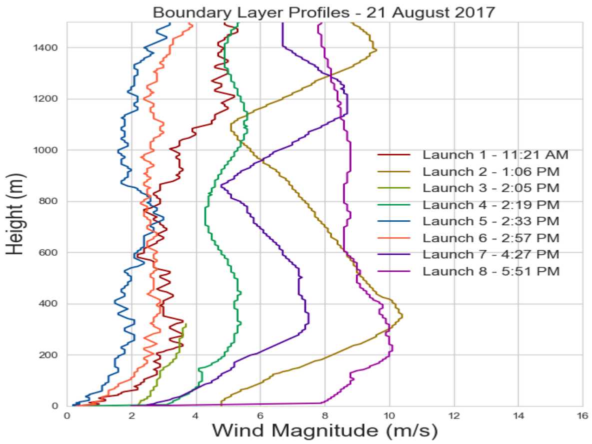

Figure 4.2: Temperature observations with height throughout the boundary layer. Profiles smoothed with low-pass median filter.

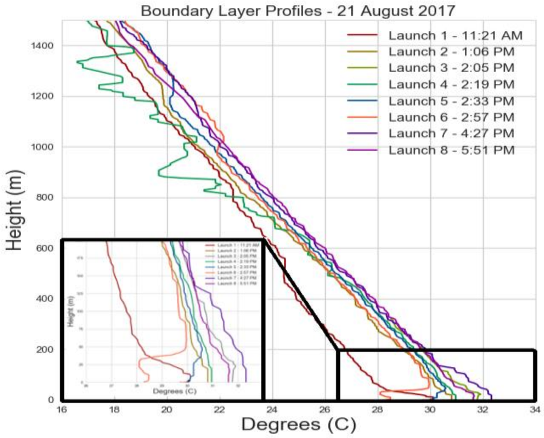

Figure 4.3: Wind magnitude with height throughout the boundary layer. Profiles smoothed using low-pass median filter.

Before first contact, the last remnants of the nocturnal boundary layer reside at the base of the profile, as temperature increases slightly up until 25 meters during Launch 1 (red). Afterwards, the temperature decreases at the environmental lapse rate before becoming isothermal around 500 meters. The temperature continues to decrease at the environmental lapse rate just before 600 meters. Launch 1 also measured wind speeds with little variability between 2-5 m/s. In first 200 meters, wind speeds are relatively consistent until 1,000 meters and then another increase at 1,000 meters. The measured profile resembles a typical mid-morning profile. Launch 2 (brown) recorded an eroding of the lowest level temperature inversion seen in launch 1. More notable are the recorded wind speeds—speeds are higher and vary between 5-10 m/s once above friction effects, with peak wind speeds at ~400 meters and 1,400 meters. Launch 3 (gray) was a truncated measurement. It displayed similar near surface temperatures, but slower winds than launch 2. During first contact and approximately twenty minutes prior to totality, launch 4 (green) recorded a slightly decreased surface temperature, which continued to decrease at the environmental lapse rate until approximately 700 meters. Beyond 700 meters, the temperature varies and oscillates, with a vertical wavelength of about 100 meters. The wind speed for this launch varied little, between 4-6 m/s. Launch 5 (blue) was taken minutes before totality and depicts a decrease in surface temperature. A surface inversion is noted as well as a weak inversion around 1,100 meters. The associated wind speed contained light winds with little variability, between 2-3 m/s. Launch 6 (orange), taken after totality and during third contact, clearly illustrates a strong low-level inversion from the surface to approximately 50 meters; afterwards, the temperature decreases at the dry adiabatic lapse rate. Continued wind patterns are between 2-3 m/s. Launch 7 (dark purple) shows a 6°C surface temperature increase compared to launch 6. Wind speeds from launch 7 are also stronger and vary between 5-9 m/s. Launch 8 (light purple) depicts a decreasing surface temperature as the sun angle continues to decrease for the time of day. Winds are stronger and most consistent between 9-10 m/s.

4.3 INTERNAL GRAIVTY WAVE MEASUREMENTS

Four radiosonde launches were used for IGW analysis, launches 1, 6, and 8, because they were able to reach the top height of the troposphere and breach into the stratosphere. Launch 5 was also used for IGW analysis because the launch was conducted during totality. A height window of 16,000-24,000 was selected to ensure assessment in the tropopause and stratosphere.

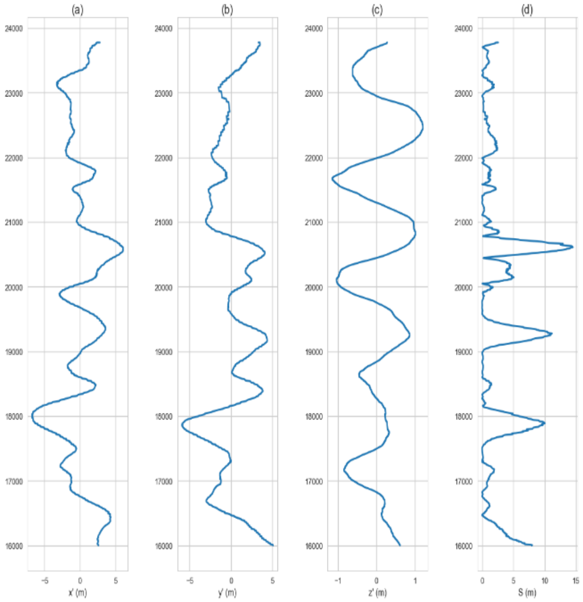

Figure 4.4: Wind perturbations for launch 1

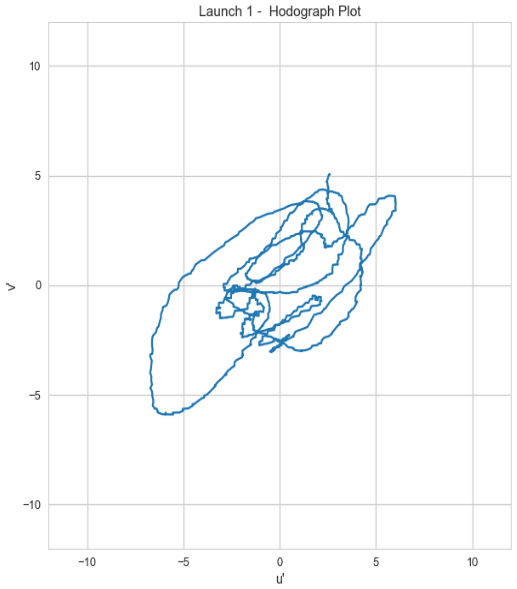

Figure 4.5: Hodograph plot for launch 1

Launch 1 – Pre-eclipse

An analysis of the perturbations in launch 1 shows peaks in parcel movement within the selected window of 16,000-24,000 meters at a vertical wavelength of 1.2 kilometers (Figure 6a, right panel). The hodograph plot depicts an ellipse oriented from the southwest to the northeast (Figure 6b). The intrinsic angular period at the local maxima 19,277 meters and 20,611 meters were calculated to be 5 minutes and 6.5 minutes, respectively.

Launch 5 – during eclipse (during totality)

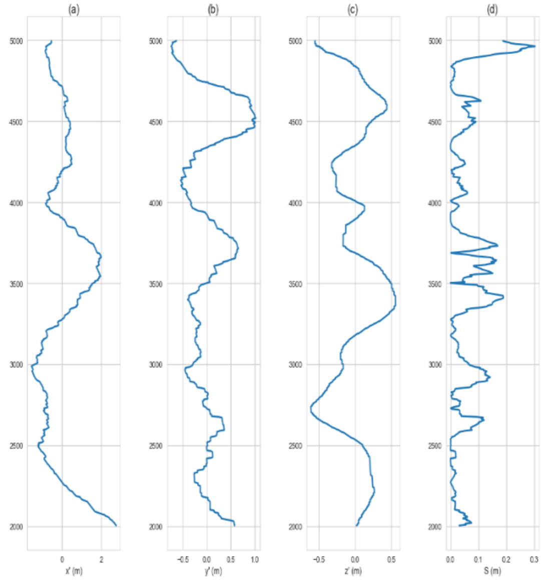

Figure 4.6: Wind perturbations for launch 5

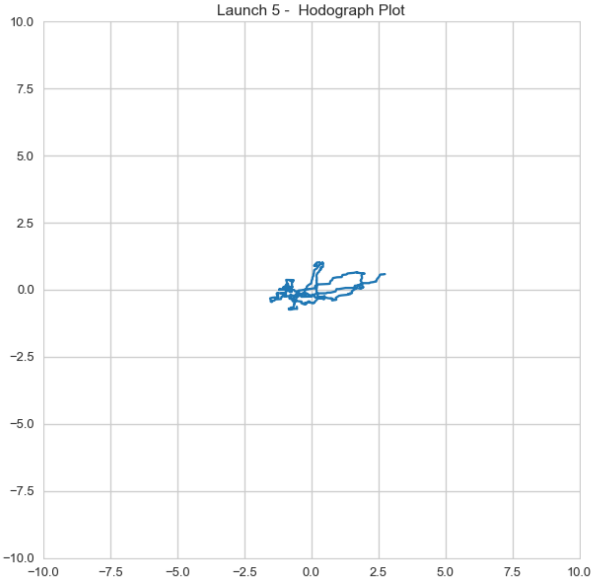

Figure 4.7: Hodograph plot for launch 5

Analysis of launch 5, launched after totality and during 3rd contact, offers insight into eclipse induced IGW. Due to loss of radio contact, the balloon was only able to ascend to 6,000 meters. This provided only a window of 2,000-5,000 for parcel analysis

(Figure 7a). A vertical wavelength of approximately 500 meters is noted (Figure 7a, right panel). The accompanying hodograph details a prominent ellipse shape oriented from southwest to northeast and very little variability (Figure 7b). However, when solving for the wave period associated with the intrinsic angular frequency, values ranging from 2-4 minutes were solved for.

Launch 6 – during eclipse (3rd contact)

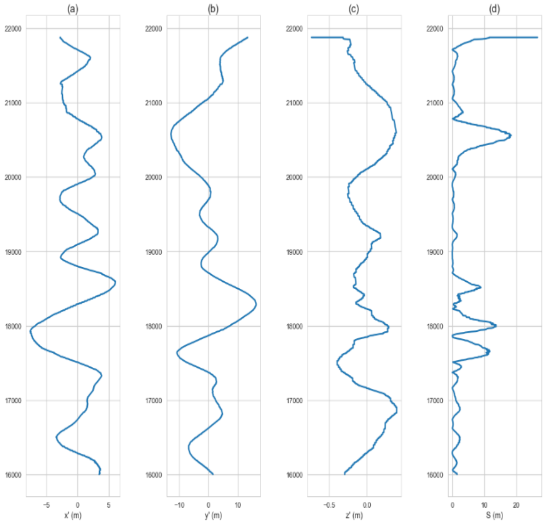

Figure 4.8: Wind perturbations for launch 6

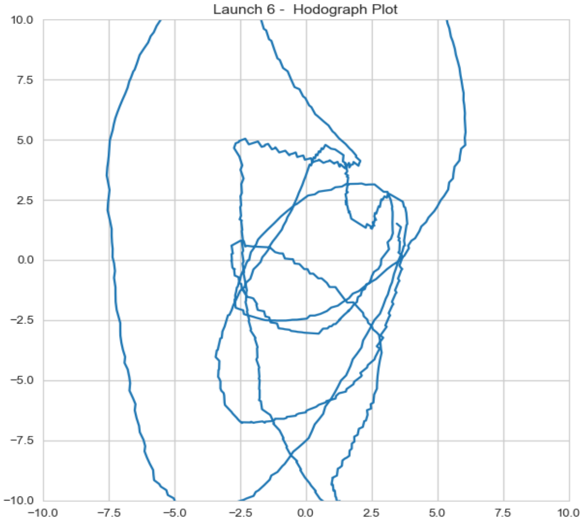

Figure 4.9: Hodograph plot for launch 6

The sixth balloon, launched during third contact, was able to ascend to projected height. By this point, it is assumed that any probable IGW induced by the eclipse still resonated in the atmosphere. The large variations in movement (Figure 8b) within the window of 16,000-22,000 meters were coupled with periods calculated from the wave's frequency ranged from 20-29 minutes. The dominant vertical wavelength is measured to be 500 meters with embedded wavelengths of approximately 330 meters from the 17,500-18,500 height window (Figure 8a, right panel).

Launch 8

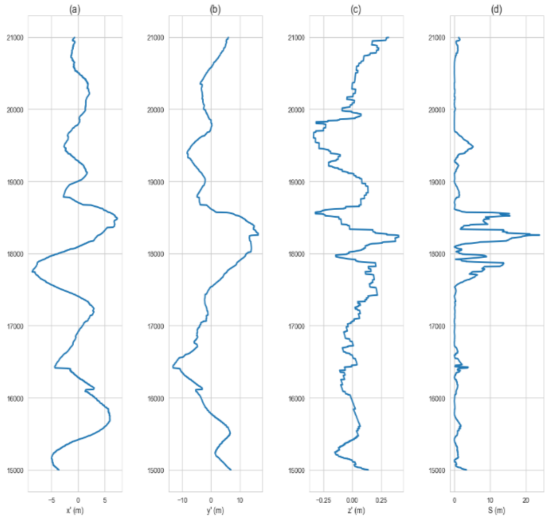

Figure 4.10: Wind perturbations for launch 8

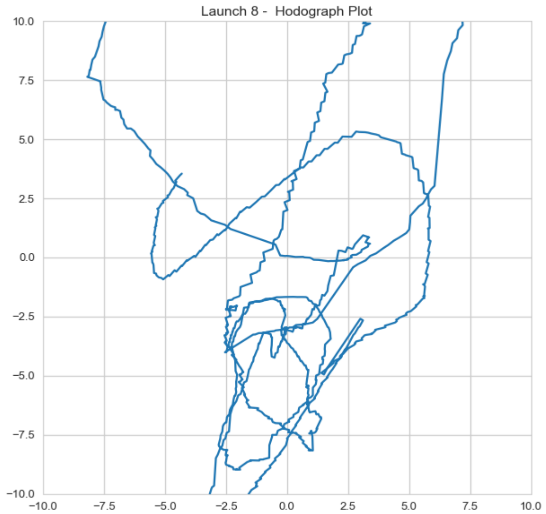

Figure 4.11: Hodograph plot for launch 8

Launch 8 perturbation profiles for the last launch depict large movement within the 16,000-21,000 minute window (Figure 9a). The hodograph analysis shows an ellipse shape orientation in the south-southwest to north-northeast direction. An analysis of Figure 9b shows a low amplitude vertical wavelength in the lower portions of the atmosphere (16,000-17,000 meters) of approximately 500 meters. Then, from the window of 17,500-18,500 meters, the IGWs appears to be much higher in amplitude and shorter in wavelength, with a value of 250 meters. Calculated periodicity ranged from 17.9-54.5 minutes.

4.4 WRF SIMULATION

To ensure an accurate comparison of observed and modeled temperature, the modeled atmospheric profile from 1000 millibars to 100 millibars is shown with the corresponding radiosonde observation (Figure 10). Overall, the model performs well with respect to temperature, with the only discrepancy at the surface. The model is shown to have a warm bias of 2°C from 943-997 millibars. Modeled dewpoint measurements were erratic and did not verify.

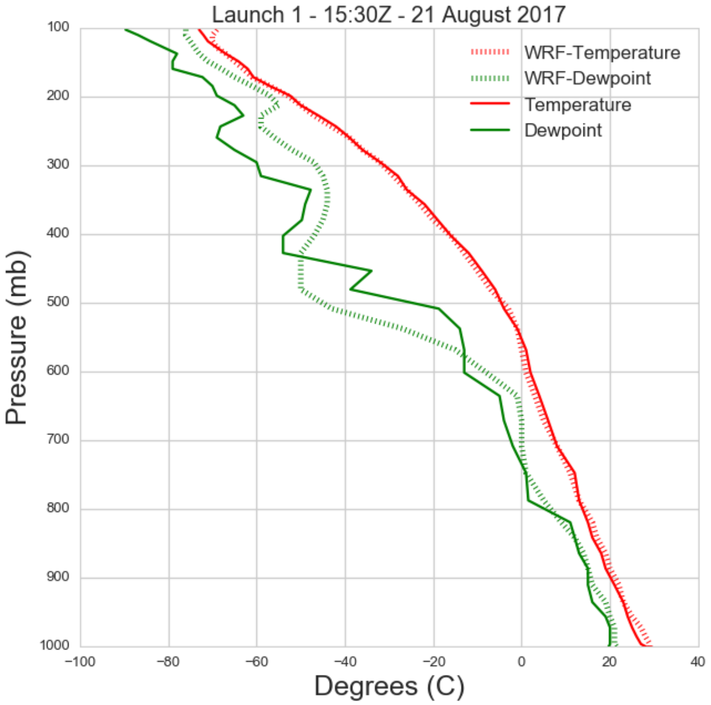

Figure 4.12: Temperature and dewpoint from launch 1 is compared to a modeled simulation for the same time frame.

To compare the modeled temperature to observed temperatures just after totality, the modeled temperatures from the surface to 850 millibars were examined at 19:00Z (3:00 PM EDT), as they most closely correspond to the fifth balloon launch which began at 18:57Z (2:57 PM EDT) (Figure 11). The result shows a large discrepancy between observed and modeled temperatures. The largest temperature difference lies at the surface, as expected, with a magnitude of approximately 4°C. Just above developing nocturnal boundary layer, the remnants of the mixed layer transition to a residual layer. In the modeled sounding, the mixed layer is still coupled to the surface.

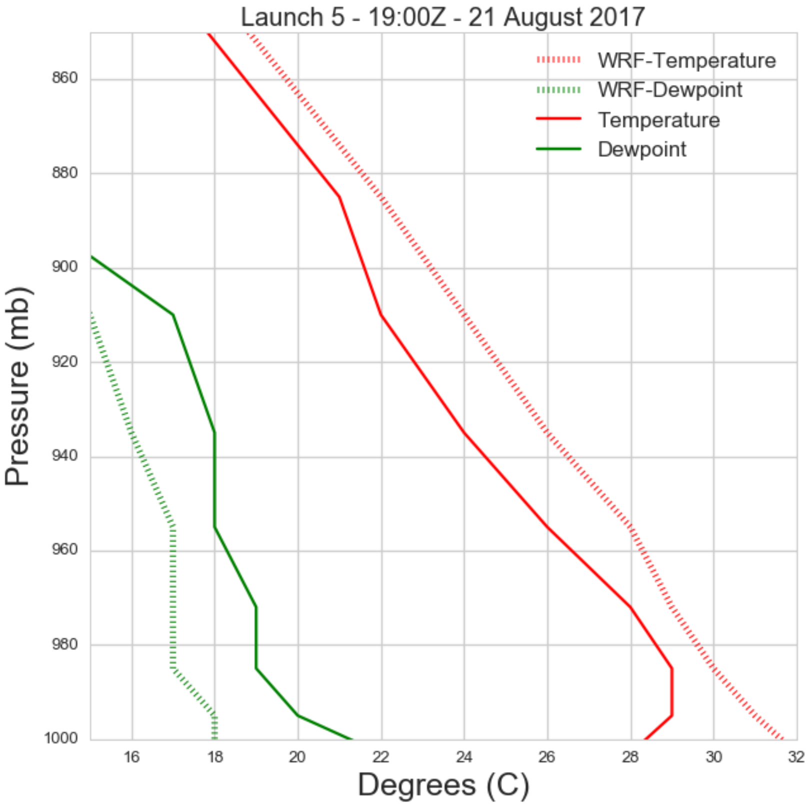

Figure 4.13: Observed and simulated boundary layer profiles shortly after totality occurred.

CHAPTER V

DISCUSSION

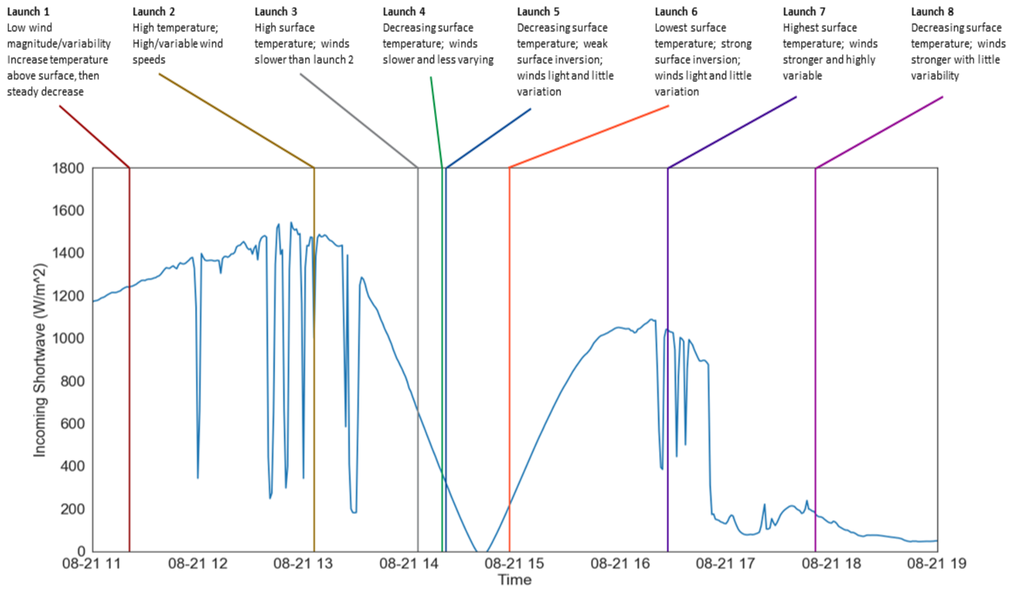

Figure 5.1: Displays the incoming shortwave radiation from 11AM-7PM EDT on 21 August 21, 2017. Associated balloon launches are marked with notes on temperature and wind magnitude measurements.

Measurements taken in the boundary layer offer insight on the progression of atmospheric variables before, during, and after a total solar eclipse. A noted observation lies in the lowest 175 meters. The layer between the surface and 175 meters seems most responsive to the change in incoming solar radiation, as temperature varies much more at this level compared to the remaining profile in all instances.

Wind speed measurements throughout the boundary layer column show variation throughout launches before, during, and after the eclipse event (Figure 12). In the morning and before the eclipse, patterns vary from a small amount of turbulence, as indicated by the little variation in wind speed, to detecting larger turbulent eddies as the next launches went into the afternoon hours. This change is likely caused by the eroding of the previous residual boundary layer and creation of the mixed layer as the Sun's heat increased mechanical mixing. During the beginnings of the eclipse and as more of the Sun's radiation was blocked from reaching the surface, a stable boundary layer was created, leading to both low wind speed and smaller variations in wind speed. After the end of the partial eclipse in the mid-to-late afternoon hours, mechanical mixing began again, leading to creation of turbulent eddies again. This explains the high wind speeds with large variations during launch 7. By launch 8, approaching 6PM EDT, the low sun angle is unable to create such mixing, allowing for the continuation of high wind speeds, but suppressing the mixing and leading to little variation in the wind speed.

Hodograph analysis depicts elliptical shapes within each of the high-altitude windows, suggesting IGW in both instances before and after the total solar eclipse. However, it is worth noting the evolution of the balloon hodographs throughout the day. Prior to the eclipse, an elliptical pattern is seen oriented in a southwest to northeast direction. Measurements taken directly after totality show a hodograph, while small in variability, oriented in the original southwest to northeast direction, but also containing a signature oriented from south to north. Fifteen minutes later, during the next profile measurement, a full south to north oriented ellipse is seen. Finally, towards the early evening hours, the last measurement shows an adjustment of the ellipse back to its original southwest to northeast orientation. Based on the evolution of the hodograph profiles, it would seem IGW were already noted within the region, likely spurred on by the convective activity to the southeast of the field location. In addition, the eclipse generated additional IGW that altered the signature, and by the evening hours, the original IGW signature had assumed the dominant role.

Wave period calculations depict a clear divide between pre-eclipse and post-eclipse. Before the eclipse, the calculated wave periods of launch 1 were between 5-6.5 minutes. Twenty minutes after totality, launch 6 returned values which were calculated to be between 20-23 minutes. The wave's periodicity here is supported by previous cases of eclipse induced IGW. The final launch comes with the assumption the atmosphere has returned to its pre-eclipse state, with IGW having dissipated. However, calculated periodicities suggest the IGWs continued to resonate as values ranged from 17-54.5 minutes, also aligning with previous studies. This is important to note due to the location of the stationary front southeast of the field location. Because severe convection can often trigger IGW, it can be hypothesized that the convection to the southeast triggered IGW of low wave period by reason of the further distance. Eclipse inducted IGW carried a much stronger wave period signature, one which muddied the signal of the morning IGW created by the stationary front's convection. By day's end, the eclipse induced IGW had dissipated, leaving convection to the southeast to be the main source of wave periodicity.

The WRF simulation of the boundary layer temperatures unaffected by the solar eclipse detail a surface temperature approximately 4°C warmer than observed temperatures just after totality. Furthermore, the residual convective mixed layer is seen in observations from 990-890 millibars compared to the modeled convective mixed layer from the surface up to 960 millibars. This discrepancy between observations during an eclipse and a model weather scenario reveals a challenge in the event of total solar eclipse events for, as the temperature discrepancy is not expected by forecast models. Model output is used by many, each carrying out their own economic operations. For example, those with vested interests in solar power must be wary of changes in temperature, as the maximum load output is dependent on this variable. This model inconsistency also has implications for those operating aircraft. Changes in the boundary layer regime offers changes in turbulence over a short period of time and has implications on safety during take-off and landing procedures. Finally, one must question the implications a total solar eclipse has on subsequent numerical weather simulations. Because models ingest observations, reduced temperatures could trickle down in subsequent model initializations and lead to erroneous model initializations and forecasts.

CHAPTER VI

CONCLUSION

This study has found evidence to suggest the 21 August 2017 total solar eclipse generated IGW. Consequences of localized convection to the southeast of the field site location could have impeded the ability to detect the IGW signal, but due to the continued observation before, during, and after the eclipse, it appears likely to have recorded both mechanisms of IGW, convection and solar eclipse. Observations noted the atmosphere’s adjustment to localized convection, readjustment to the eclipse, and returning of its pre-eclipse state by the early evening hours. The evolution of the IGW wave periods throughout the day suggest a clear impact of the total solar eclipse on the development of internal gravity waves, as calculated wave periods after totality fall in line with previous eclipse studies on IGW.

A modeling effort revealed significant inconsistencies in both temperature and moisture variables, which has the possibility of trickling down into subsequent numerical simulations and ultimately lead to incorrect model initialization and error in forecasts. While rare events, models need to be able to account for such drastic change in atmospheric profiles to prevent future weather predictions and allow for correct information to be ingested by audiences utilizing it for safety procedures and economic prosperity.

To expand upon this area of research, the total solar eclipse of 8 April 2024 allows an advantage not afforded in previous studies. Due to the time of year in North America, convective storms less likely along the eclipse path of totality and allow for more pure observations to take place. Furthermore, a recent effort was conducted to model the consequences of the eclipse event on 21 August 2017. Recently, the NOAA Global Systems Division (GSD) and the Cooperative Institute for Research in Environmental Sciences (CIRES) adopted an algorithm using Bessel's method to account for the blocking of the solar disc to anticipate the WRF model's response to the eclipse (Olson *et al.*, 2017). The eclipse in 2024 allows for time to test and validate the model's method to accurately predict atmospheric variables.

REFERENCES

Anderson, J. (1999). Meteorological changes during a solar eclipse. *Weather*, *54*(1997), 207–215. https://doi.org/10.1002/j.1477-8696.1999.tb06465.x

Anderson, R. C., & Keefer, D. R. (1975). Observation of the Temperature and Pressure Changes During the 30 June 1973 Solar Eclipse. *Journal of Atmospheric Sciences*, *32*, 228–231. https://doi.org/https://doi.org/10.1175/1520-0469(1975)032<0228:OOTTAP>2.0.CO;2

Anderson, R. C., Keefer, D. R., & Myers, O. E. (1972). Atmospheric Pressure and Temperature Changes During the 7 March 1970 Solar Eclipse.

Aplin, K. L., Scott, C. J., & Gray, S. L. (2016). Atmospheric changes from solar eclipses. *Philosophical Transactions. Series A, Mathematical, Physical, and Engineering Sciences*, *374*(2077), 20150217. https://doi.org/10.1098/rsta.2015.0217

Aplin, K. L., & Harrison, R. G. (2002). Meteorological effects of the eclipse of 11 August 1999 in cloudy and clear conditions. *The Royal Society*, *459*(2030), 353–371. https://doi.org/https://doi.org/10.1098/rspa.2002.1042

Clayton, H. H.: The eclipse cyclone and the diurnal cyclones, Ann. Astron. Observ. Harvard College, 43, 5–33, 1901.

Chimonas, G., & Hines, C. O. (1971). Atmospheric gravity waves induced by a solar eclipse, 2. *Journal of Geophysical Research*, *76*(28), 7003.

https://doi.org/10.1029/JA076i028p07003

Collier, C. G. (2006). The impact of urban areas on weather. *Quarterly Journal of the Royal Meteorological Society*, *132*(614), 1–25. https://doi.org/10.1256/qj.05.199

Eaton, F. D. (1997). Solar eclipse effects observed in the planetary boundary layer over a desert, 331–346.

Eaton, F. D., Hines, J. R., Hatch, W. H., Cionco, R. M., Byers, J., Garvey, D., & Miller, D. R. (1997). Solar Eclipse Effects Observed in the Planetary Boundary Layer Over a Desert. *Boundary-Layer Meteorology*, *83*(2), 331–346. https://doi.org/10.1023/A:1000219210055

Founda, D., Melas, D., Lykoudis, S., Lisaridis, I., Gerasopoulos, E., Kouvarakis, G., … Zerefos, C. (2007). The effect of the total solar eclipse of 29 March 2006 on meteorological variables in Greece. *Atmospheric Chemistry and Physics Discussions*, *7*(4), 10631–10667. https://doi.org/10.5194/acpd-7-10631-2007

Fritts, D. C. (2003). Gravity wave dynamics and effects in the middle atmosphere. *Reviews of Geophysics*. https://doi.org/10.1029/2001RG000106

Gray, S. L., & Harrison, R. G. (2016). Eclipse-induced wind changes over the British Isles on the 20 March 2015, *374*(2077). https://doi.org/10.1098/rsta.2015.0224

Hobson, G.L. Goodwin and G.J., S. A. I. of T. (1978). Atmospheric gravity waves generated during a solar eclipse.

Kimball, H., & Fergusson, S. P. (1919). Influence of the solar eclipse of June 8, 1918, upon radiation and others meteorological elements. *Monthly Weather Review*, (January), 5–16.

Krishnan, P., Kunhikrishnan, P. K., Nair, S. M., Ravindran, S., Ramachandran, R., Subrahamanyam, D. B., & Ramana, M. V. (2004). Observations of the atmospheric surface layer parameters August 11th , 1999. *Proc. Indian Acad. Sci. (Earth Planet. Sci.), 113*(3), 353–363.

Marlton, G. J., Williams, P. D., & Nicoll, K. A. (2016). On the detection and attribution of gravity waves generated by the 20 March 2015 solar eclipse Subject Areas :, (March).

Paramitha, B., Zaen, R., & Nandiyanto, A. B. D. (2017). Changes in Meteorological Parameters (i.e. UV and Solar Radiation, Air Temperature, Humidity and Wind Condition) during the Partial Solar Eclipse of 9 March 2016. *IOP Conference Series: Materials Science and Engineering*, *180*, 12131. https://doi.org/10.1088/1757-899X/180/1/012131

Sandford, S. A., Bernstein, M. P., & Materese, C. K. (2013). NASA Public Access. *Astrophys J Suppl Ser.*, *205*(1), 1–58. https://doi.org/10.1088/0067-0049/205/1/8.The

Vincent, R. A., & Alexander, M. J. (2000). Gravity waves in the tropical lower stratosphere: observational study of seasonal and interannual variability. *Journal of Geophysical Research*, *105*(D14), 17971–17982.

Zerefos, C. S., Gerogiannis, V. T., Balis, D., Zerefos, S. C., & Kazantzidis, A. (2007). Atmospheric effects of volcanic eruptions as seen by famous artists and depicted in their paintings. *Atmos. Chem. Phys. Atmospheric Chemistry and Physics*, *7*(1980), 4027–4042. https://doi.org/10.5194/acpd-7-5145-2007

APPENDIX A

WRF PARAMETERIZATION OF SHORTWAVE RADIATION

Because total solar eclipse events alter the meteorological variables under the moon's shadow and lead to different circumstances later in the day, an attempt to calibrate WRF to account for the total solar eclipse was performed. Because WRF is not outfitted to predict such a change in incoming shortwave radiation, the radiation scheme housed in WRF's radiation physics package (module_ra_sw.F) was altered to account for the change during the total solar eclipse (hereafter WRF-Eclipse) and has been adapted from Founda *et al*. (2007). To achieve this, a line of best fit representing the path of totality was first created across the model domain (Equations 8, 9), where *X* is the time in minutes when the eclipse event begins subtracted from the number of minutes after model initialization. Path coordinates were found from https://eclipse.gsfc.nasa.gov/SEpath/SEpath2001/SE2017Aug21Tpath.html. Equation 10 serves as the linear increase in shortwave radiation outward from totality to account for locations experiencing some percentage of solar obscuration.

Eq 8

$$\text{SHADOWLONG} = 0.3728\text{X} - 132.62$$

Eq 9

$$\text{SHADOWLAT} = -0.1774\text{X} + 58.321$$

Eq 10

$$\text{PER} = \frac{(-0.0233 \times \text{SDISTAN} + 100)}{100}$$

These equations allow for a total eclipse "shadow" to move across the domain inside WRF-Eclipse, calling for zero shortwave radiation along areas under the path of totality and a linear increase as distance increases away from the center line. A modeled sounding is then extracted from the location of the radiosonde launches for comparison as well as validate the model's effectiveness in simulating temperature, dewpoint, and wind speed and direction during a solar eclipse event. Due to a difference in model version, the results of the WRF-Eclipse run were inconclusive. Founda *et al.* (2007) used WRF 2.1.2 whereas this study used the updated 3.9.1. While updated versions usually include more accurate approaches to equations to resolve chaotic atmospheric variables, the main difference between the two of these versions seems to lie in script architecture. In that, the instructions called to resolved incoming shortwave radiation are executed in a different manner or require unknown dependencies not originally addressed in Founda *et al.* (2007). The attempted script is provided in Appendix B, with the portion dedicated to parameterizing the eclipse highlighted in red.

APPENDIX B

WRF SHORTWAVE RADIATION PACKAGE ADJUSTED FOR ECLIPSE PATH

```
!WRF:MODEL_LAYER:PHYSICS
!
MODULE module_ra_sw

      REAL,PRIVATE,SAVE :: CSSCA

CONTAINS

!------------------------------------------------------------------
   SUBROUTINE SWRAD(dt,RTHRATEN,GSW,XLAT,XLONG,ALBEDO,            &
                    rho_phy,T3D,QV3D,QC3D,QR3D,                   &
                    QI3D,QS3D,QG3D,P3D,pi3D,dz8w,GMT,             &
                    R,CP,G,JULDAY,                                &
                    XTIME,DECLIN,SOLCON,                          &
                    F_QV,F_QC,F_QR,F_QI,F_QS,F_QG,                &
                    pm2_5_dry,pm2_5_water,pm2_5_dry_ec,           &
                    RADFRQ,ICLOUD,DEGRAD,warm_rain,               &
                    ids,ide, jds,jde, kds,kde,                    &
                    ims,ime, jms,jme, kms,kme,                    &
                    its,ite, jts,jte, kts,kte,                    &
                    coszen,julian                                 & ! jararias, 14/08/2013
                    )
!------------------------------------------------------------------
   IMPLICIT NONE
!------------------------------------------------------------------
   INTEGER,    INTENT(IN   ) ::        ids,ide, jds,jde, kds,kde, &
                                       ims,ime, jms,jme, kms,kme, &
                                       its,ite, jts,jte, kts,kte

   LOGICAL,    INTENT(IN   ) ::        warm_rain
   INTEGER,    INTENT(IN   ) ::        icloud

   REAL, INTENT(IN    )      ::        RADFRQ,DEGRAD,             &
                                       XTIME,DECLIN,SOLCON
!
   REAL, DIMENSION( ims:ime, kms:kme, jms:jme ),                  &
         INTENT(IN    ) ::                                   P3D, &
                                                            pi3D, &
                                                         rho_phy, &
                                                            dz8w, &
                                                             T3D
   REAL, DIMENSION( ims:ime, kms:kme, jms:jme ), OPTIONAL ,       &
         INTENT(IN    ) ::                             pm2_5_dry, &
                                                     pm2_5_water, &
                                                    pm2_5_dry_ec


   REAL, DIMENSION( ims:ime, kms:kme, jms:jme ),                  &
         INTENT(INOUT)  ::                              RTHRATEN
!
   REAL, DIMENSION( ims:ime, jms:jme ),                           &
         INTENT(IN   )  ::                                  XLAT, &
                                                           XLONG,
```

```
                                                          ALBEDO
!
   REAL, DIMENSION( ims:ime, jms:jme ),                           &
         INTENT(INOUT)  ::                                     GSW
!
   REAL, INTENT(IN   )   ::                          GMT,R,CP,G,dt
!
   INTEGER, INTENT(IN  ) ::                               JULDAY

   ! --- jararias 14/08/2013
   REAL, DIMENSION( ims:ime, jms:jme ), OPTIONAL, INTENT(IN) :: COSZEN
   REAL, OPTIONAL, INTENT(IN) :: JULIAN

!
! Optional
!
   REAL, DIMENSION( ims:ime, kms:kme, jms:jme ),                  &
         OPTIONAL,                                                &
         INTENT(IN    ) ::                                        &
                                                            QV3D, &
                                                            QC3D, &
                                                            QR3D, &
                                                            QI3D, &
                                                            QS3D, &
                                                            QG3D

   LOGICAL, OPTIONAL, INTENT(IN )      ::        F_QV,F_QC,F_QR,F_QI,F_QS,F_QG

! LOCAL VARS

   REAL, DIMENSION( kts:kte ) ::                                  &
                                                          TTEN1D, &
                                                          RHO01D, &
                                                             P1D, &
                                                              DZ, &
                                                             T1D, &
                                                            QV1D, &
                                                            QC1D, &
                                                            QR1D, &
                                                            QI1D, &
                                                            QS1D, &
                                                            QG1D
!
   REAL::      XLAT0,XLONG0,ALB0,GSW0

!
   INTEGER :: i,j,K,NK
   LOGICAL :: predicate , do_topo_shading
   real :: aer_dry1(kts:kte),aer_water1(kts:kte)

!------------------------------------------------------------------

   j_loop: DO J=jts,jte
   i_loop: DO I=its,ite

! reverse vars
         DO K=kts,kte
            QV1D(K)=0.
            QC1D(K)=0.
            QR1D(K)=0.
            QI1D(K)=0.
            QS1D(K)=0.
            QG1D(K)=0.
         ENDDO

         DO K=kts,kte
            NK=kme-1-K+kms
            TTEN1D(K)=0.
```

```
            T1D(K)=T3D(I,NK,J)
            P1D(K)=P3D(I,NK,J)
            RHO01D(K)=rho_phy(I,NK,J)
            DZ(K)=dz8w(I,NK,J)
         ENDDO

         IF( PRESENT(pm2_5_dry) .AND. PRESENT(pm2_5_water) )THEN
            DO K=kts,kte
               NK=kme-1-K+kms
               aer_dry1(k)   = pm2_5_dry(i,nk,j)
               aer_water1(k) = pm2_5_water(i,nk,j)
            ENDDO
         ELSE
            DO K=kts,kte
               aer_dry1(k)   = 0.
               aer_water1(k) = 0.
            ENDDO
         ENDIF

         IF (PRESENT(F_QV) .AND. PRESENT(QV3D)) THEN
            IF (F_QV) THEN
               DO K=kts,kte
                  NK=kme-1-K+kms
                  QV1D(K)=QV3D(I,NK,J)
                  QV1D(K)=max(0.,QV1D(K))
               ENDDO
            ENDIF
         ENDIF

         IF (PRESENT(F_QC) .AND. PRESENT(QC3D)) THEN
            IF (F_QC) THEN
               DO K=kts,kte
                  NK=kme-1-K+kms
                  QC1D(K)=QC3D(I,NK,J)
                  QC1D(K)=max(0.,QC1D(K))
               ENDDO
            ENDIF
         ENDIF

         IF (PRESENT(F_QR) .AND. PRESENT(QR3D)) THEN
            IF (F_QR) THEN
               DO K=kts,kte
                  NK=kme-1-K+kms
                  QR1D(K)=QR3D(I,NK,J)
                  QR1D(K)=max(0.,QR1D(K))
               ENDDO
            ENDIF
         ENDIF

!
         IF ( PRESENT( F_QI ) ) THEN
            predicate = F_QI
         ELSE
            predicate = .FALSE.
         ENDIF

         IF ( predicate .AND. PRESENT( QI3D ) ) THEN
            DO K=kts,kte
               NK=kme-1-K+kms
               QI1D(K)=QI3D(I,NK,J)
               QI1D(K)=max(0.,QI1D(K))
            ENDDO
         ELSE
            IF (.not. warm_rain) THEN
               DO K=kts,kte
               IF(T1D(K) .lt. 273.15) THEN
                  QI1D(K)=QC1D(K)
                  QC1D(K)=0.
```

```
                  QS1D(K)=QR1D(K)
                  QR1D(K)=0.
               ENDIF
               ENDDO
            ENDIF
         ENDIF

         IF (PRESENT(F_QS) .AND. PRESENT(QS3D)) THEN
            IF (F_QS) THEN
               DO K=kts,kte
                  NK=kme-1-K+kms
                  QS1D(K)=QS3D(I,NK,J)
                  QS1D(K)=max(0.,QS1D(K))
               ENDDO
            ENDIF
         ENDIF

         IF (PRESENT(F_QG) .AND. PRESENT(QG3D)) THEN
            IF (F_QG) THEN
               DO K=kts,kte
                  NK=kme-1-K+kms
                  QG1D(K)=QG3D(I,NK,J)
                  QG1D(K)=max(0.,QG1D(K))
               ENDDO
            ENDIF
         ENDIF

         XLAT0=XLAT(I,J)
         XLONG0=XLONG(I,J)
         ALB0=ALBEDO(I,J)
! slope code removed - factor now done in surface driver
           CALL SWPARA(TTEN1D,GSW0,XLAT0,XLONG0,ALB0,              &
                       T1D,QV1D,QC1D,QR1D,QI1D,QS1D,QG1D,P1D,      &
                       XTIME,GMT,RHO01D,DZ,                        &
                       R,CP,G,DECLIN,SOLCON,                       &
                       RADFRQ,ICLOUD,DEGRAD,aer_dry1,aer_water1,   &
                       kts,kte,                                    &
                       coszen(i,j),julian                          ) ! jararias, 14/08/2013
         GSW(I,J)=GSW0
         DO K=kts,kte
            NK=kme-1-K+kms
            RTHRATEN(I,K,J)=RTHRATEN(I,K,J)+TTEN1D(NK)/pi3D(I,K,J)
         ENDDO
!
   ENDDO i_loop
   ENDDO j_loop

   END SUBROUTINE SWRAD

!------------------------------------------------------------------
   SUBROUTINE SWPARA(TTEN,GSW,XLAT,XLONG,ALBEDO,               &
                     T,QV,QC,QR,QI,QS,QG,P,                    &
                     XTIME, GMT, RHO0, DZ,                     &
                     R,CP,G,DECLIN,SOLCON,                     &
                     RADFRQ,ICLOUD,DEGRAD,aer_dry1,aer_water1, &
                     kts,kte,coszen,julian,                    &
                     slope_rad,shadow,slp_azi,slope            )
!------------------------------------------------------------------
!     TO CALCULATE SHORT-WAVE ABSORPTION AND SCATTERING IN CLEAR
!     AIR AND REFLECTION AND ABSORPTION IN CLOUD LAYERS (STEPHENS,
!     1984)
!     CHANGES:
!       REDUCE EFFECTS OF ICE CLOUDS AND PRECIP ON LIQUID WATER PATH
!       ADD EFFECT OF GRAUPEL
!------------------------------------------------------------------

  IMPLICIT NONE

  INTEGER, INTENT(IN ) ::                 kts,kte
```

```
!
  REAL, DIMENSION( kts:kte ), INTENT(IN   )  ::                   &
                                                            RHO0, &
                                                               T, &
                                                               P, &
                                                              DZ, &
                                                              QV, &
                                                              QC, &
                                                              QR, &
                                                              QI, &
                                                              QS, &
                                                              QG

   REAL, DIMENSION( kts:kte ), INTENT(INOUT)::              TTEN
!
   REAL, INTENT(IN  )   ::               XTIME,GMT,R,CP,G,DECLIN, &
                                        SOLCON,XLAT,XLONG,ALBEDO, &
                                                  RADFRQ, DEGRAD

   REAL, OPTIONAL, INTENT(IN) :: COSZEN, JULIAN ! jararias, 14/08/2013

!
   INTEGER, INTENT(IN) :: icloud
   REAL, INTENT(INOUT)  ::                                   GSW
! For slope-dependent radiation

   INTEGER, OPTIONAL, INTENT(IN) :: slope_rad,shadow
   REAL, OPTIONAL,    INTENT(IN) :: slp_azi,slope

! LOCAL VARS
!
   REAL, DIMENSION( kts:kte+1 ) ::                         SDOWN

   REAL, DIMENSION( kts:kte )   ::                          XLWP, &
                                                                             XATP, &
                                                                             XWVP, &
                                             aer_dry1,aer_water1, &
                                                                               RO
!
   REAL, DIMENSION( 4, 5 ) ::                             ALBTAB, &
                                                          ABSTAB

   REAL, DIMENSION( 4    ) ::                             XMUVAL

   REAL :: beta

!------------------------------------------------------------------

      DATA ALBTAB/0.,0.,0.,0., &
           69.,58.,40.,15.,    &
           90.,80.,70.,60.,    &
           94.,90.,82.,78.,    &
           96.,92.,85.,80./

      DATA ABSTAB/0.,0.,0.,0., &
           0.,2.5,4.,5.,       &
           0.,2.6,7.,10.,      &
           0.,3.3,10.,14.,     &
           0.,3.7,10.,15./

      DATA XMUVAL/0.,0.2,0.5,1.0/

        GSW=0.0
              OPEN (9,FILE='SOLARCONSTANT')
              IF ((XTIME.GE.1165) .AND. (XTIME.LE.1400)) THEN
               TIM=XTIME-1165
               SHADOWLONG=0.03728*TIM-132.62
               SHADOWLAT=-0.1774*TIM+58.321
               LONDIS=(SHADOWLONG-XLONG)**2
```

```
               LATDIS=(SHADOWLAT-XLAT)**2
               SDISTAN=(SQRT(LONDIS+LATDIS))*110
            IF (SDISTAN.LT.57) THEN
                 WRITE(9,*) XTIME,XLONG,XLAT
                 GOTO 7
               ELSEIF (SDISTAN.LT.4000) THEN
                PER=(-0.0233*SDISTAN+100)/100
                SOLTOP=SOLCON*PER
                WRITE(9,*) XTIME,XLONG,XLAT,SOLTOP
                ELSE
                SOLTOP=SOLCON
             ENDIF
              ELSE
               SOLTOP=SOLCON
              ENDIF

      REAL :: bext340, absc, alba, alw, csza,dabsa,dsca,dabs
      REAL :: bexth2o, dscld, hrang,ff,oldalb,oldabs,oldabc
      REAL :: soltop, totabs, tloctm, ugcm, uv,xabs,xabsa,wv
      REAL :: wgm, xalb, xi, xsca, xt24,xmu,xabsc,trans0,yj
      REAL :: xxlat,ww
      INTEGER :: iil,ii,jjl,ju,k,iu
      REAL :: da,eot ! jararias 14/08/2013

! For slope-dependent radiation

   REAL :: diffuse_frac, corr_fac, csza_slp

       GSW=0.0
       bext340=5.E-6
       bexth2o=5.E-6
       SOLTOP=SOLCON
       ! jararias, 14/08/2013
       if (present(coszen)) then
          csza=coszen
       else
!         da=6.2831853071795862*(julian-1)/365.
!         eot=(0.000075+0.001868*cos(da)-0.032077*sin(da) &
!            -0.014615*cos(2*da)-0.04089*sin(2*da))*(229.18)
          xt24 = mod(xtime+radfrq*0.5,1440.)+eot
          tloctm = gmt + xt24/60. + xlong/15.
          hrang = 15. * (tloctm-12.) * degrad
          xxlat = xlat * degrad
          csza = sin(xxlat) * sin(declin) &
               + cos(xxlat) * cos(declin) * cos(hrang)
       end if

!     RETURN IF NIGHT
      IF(CSZA.LE.1.E-9)GOTO 7
!
      DO K=kts, kte

! P in the unit of 10mb
         RO(K)=P(K)/(R*T(K))
         XWVP(K)=RO(K)*QV(K)*DZ(K)*1000.
! KG/M**2
          XATP(K)=RO(K)*DZ(K)
      ENDDO
!
!     G/M**2
!     REDUCE WEIGHT OF LIQUID AND ICE IN SHORT-WAVE SCHEME
!     ADD GRAUPEL EFFECT (ASSUMED SAME AS RAIN)
!
      IF (ICLOUD.EQ.0)THEN
         DO K=kts, kte
            XLWP(K)=0.
         ENDDO
      ELSE
         DO K=kts, kte
```

```
            XLWP(K)=RO(K)*1000.*DZ(K)*(QC(K)+0.1*QI(K)+0.05* &
                    QR(K)+0.02*QS(K)+0.05*QG(K))
         ENDDO
      ENDIF
!
      XMU=CSZA
      SDOWN(1)=SOLTOP*XMU
!     SET WW (G/M**2) LIQUID WATER PATH INTEGRATED DOWN
!     SET UV (G/M**2) WATER VAPOR PATH INTEGRATED DOWN
      WW=0.
      UV=0.
      OLDALB=0.
      OLDABC=0.
      TOTABS=0.
!     CONTRIBUTIONS DUE TO CLEAR AIR AND CLOUD
      DSCA=0.
      DABS=0.
      DSCLD=0.
!
! CONTRIBUTION DUE TO AEROSOLS (FOR CHEMISTRY)
      DABSA=0.
!
      DO 200 K=kts,kte
         WW=WW+XLWP(K)
         UV=UV+XWVP(K)
!     WGM IS WW/COS(THETA) (G/M**2)
!     UGCM IS UV/COS(THETA) (G/CM**2)
         WGM=WW/XMU
         UGCM=UV*0.0001/XMU
!
         OLDABS=TOTABS
!     WATER VAPOR ABSORPTION AS IN LACIS AND HANSEN (1974)
         TOTABS=2.9*UGCM/((1.+141.5*UGCM)**0.635+5.925*UGCM)
!     APPROXIMATE RAYLEIGH + AEROSOL SCATTERING
!        XSCA=1.E-5*XATP(K)/XMU
!          XSCA=(1.E-5*XATP(K)+aer_dry1(K)*bext340+aer_water1(K)*bexth2o)/XMU
         beta=0.4*(1.0-XMU)+0.1
!     CSSCA - CLEAR-SKY SCATTERING SET FROM NAMELIST SWRAD_SCAT
         XSCA=(cssca*XATP(K)+beta*aer_dry1(K)*bext340*DZ(K) &
              +beta*aer_water1(K)*bexth2o*DZ(K))/XMU

!     LAYER VAPOR ABSORPTION DONE FIRST
         XABS=(TOTABS-OLDABS)*(SDOWN(1)-DSCLD-DSCA-DABSA)/SDOWN(K)
!rs   AEROSOL ABSORB (would be elemental carbon). So far XABSA = 0.
         XABSA=0.
         IF(XABS.LT.0.)XABS=0.
!
         ALW=ALOG10(WGM+1.)
         IF(ALW.GT.3.999)ALW=3.999
!
         DO II=1,3
            IF(XMU.GT.XMUVAL(II))THEN
              IIL=II
              IU=II+1
              XI=(XMU-XMUVAL(II))/(XMUVAL(II+1)-XMUVAL(II))+FLOAT(IIL)
            ENDIF
         ENDDO
!
         JJL=IFIX(ALW)+1
         JU=JJL+1
         YJ=ALW+1.
!     CLOUD ALBEDO
         ALBA=(ALBTAB(IU,JU)*(XI-IIL)*(YJ-JJL)   &
              +ALBTAB(IIL,JU)*(IU-XI)*(YJ-JJL)   &
              +ALBTAB(IU,JJL)*(XI-IIL)*(JU-YJ)   &
              +ALBTAB(IIL,JJL)*(IU-XI)*(JU-YJ))  &
             /((IU-IIL)*(JU-JJL))
!     CLOUD ABSORPTION
         ABSC=(ABSTAB(IU,JU)*(XI-IIL)*(YJ-JJL)   &
```

```
              +ABSTAB(IIL,JU)*(IU-XI)*(YJ-JJL)   &
              +ABSTAB(IU,JJL)*(XI-IIL)*(JU-YJ)   &
              +ABSTAB(IIL,JJL)*(IU-XI)*(JU-YJ))  &
             /((IU-IIL)*(JU-JJL))
!     LAYER ALBEDO AND ABSORPTION
         XALB=(ALBA-OLDALB)*(SDOWN(1)-DSCA-DABS)/SDOWN(K)
         XABSC=(ABSC-OLDABC)*(SDOWN(1)-DSCA-DABS)/SDOWN(K)
         IF(XALB.LT.0.)XALB=0.
         IF(XABSC.LT.0.)XABSC=0.
         DSCLD=DSCLD+(XALB+XABSC)*SDOWN(K)*0.01
         DSCA=DSCA+XSCA*SDOWN(K)
         DABS=DABS+XABS*SDOWN(K)
         DABSA=DABSA+XABSA*SDOWN(K)
         OLDALB=ALBA
         OLDABC=ABSC
!     LAYER TRANSMISSIVITY
         TRANS0=100.-XALB-XABSC-XABS*100.-XSCA*100.
         IF(TRANS0.LT.1.)THEN
           FF=99./(XALB+XABSC+XABS*100.+XSCA*100.)
           XALB=XALB*FF
           XABSC=XABSC*FF
           XABS=XABS*FF
           XSCA=XSCA*FF
           TRANS0=1.
         ENDIF
         SDOWN(K+1)=AMAX1(1.E-9,SDOWN(K)*TRANS0*0.01)
         TTEN(K)=SDOWN(K)*(XABSC+XABS*100.+XABSA*100.)*0.01/( &
                 RO(K)*CP*DZ(K))
  200   CONTINUE
!
        GSW=(1.-ALBEDO)*SDOWN(kte+1)

    IF (PRESENT(slope_rad)) THEN
! Slope-dependent solar radiation part

      if (slope_rad.eq.1) then

!  Parameterize diffuse fraction of global solar radiation as a function of the ratio between TOA
radiation and surface global radiation

        diffuse_frac = min(1.,1/(max(0.1,2.1-2.8*log(log(SDOWN(kts)/max(SDOWN(kte+1),1.e-3))))))
        if ((slope.eq.0).or.(diffuse_frac.eq.1).or.(csza.lt.1.e-2)) then  ! no topographic effects
when all radiation is diffuse or the sun is too close to the horizon
        corr_fac = 1
        goto 140
        endif

! cosine of zenith angle over sloping topography

        csza_slp = ((SIN(XXLAT)*COS(HRANG))*                                          &
                    (-cos(slp_azi)*sin(slope))-SIN(HRANG)*(sin(slp_azi)*sin(slope))+  &
                    (COS(XXLAT)*COS(HRANG))*cos(slope))*                              &
                   COS(DECLIN)+(COS(XXLAT)*(cos(slp_azi)*sin(slope))+                 &
                   SIN(XXLAT)*cos(slope))*SIN(DECLIN)
        IF(csza_slp.LE.1.E-4) csza_slp = 0

! Topographic shading

        if (shadow.eq.1) csza_slp = 0

! Correction factor for sloping topography; the diffuse fraction of solar radiation is assumed to
be unaffected by the slope
        corr_fac = diffuse_frac + (1-diffuse_frac)*csza_slp/csza

 140       continue

        GSW=(1.-ALBEDO)*SDOWN(kte+1)*corr_fac

      endif
```

```
    ENDIF

    7 CONTINUE
!
   END SUBROUTINE SWPARA

!====================================================================
   SUBROUTINE swinit(swrad_scat,                                    &
                     allowed_to_read ,                              &
                     ids, ide, jds, jde, kds, kde,                  &
                     ims, ime, jms, jme, kms, kme,                  &
                     its, ite, jts, jte, kts, kte                   )
!--------------------------------------------------------------------
   IMPLICIT NONE
!--------------------------------------------------------------------
   LOGICAL , INTENT(IN)           :: allowed_to_read
   INTEGER , INTENT(IN)           :: ids, ide, jds, jde, kds, kde,  &
                                     ims, ime, jms, jme, kms, kme,  &
                                     its, ite, jts, jte, kts, kte

   REAL , INTENT(IN)              :: swrad_scat

!     CSSCA - CLEAR-SKY SCATTERING SET FROM NAMELIST SWRAD_SCAT
   cssca = swrad_scat * 1.e-5

   END SUBROUTINE swinit


END MODULE module_ra_sw
```